

# In-flight performance and calibration of SPICAV SOIR onboard Venus Express

Arnaud Mahieux,<sup>1,\*</sup> Sophie Berkenbosch,<sup>1</sup> Roland Clairquin,<sup>1</sup> Didier Fussen,<sup>1</sup>  
Nina Mateshvili,<sup>1</sup> Eddy Neefs,<sup>1</sup> Dennis Nevejans,<sup>1,2</sup> Bojan Ristic,<sup>1</sup>  
Ann Carine Vandaele,<sup>1</sup> Valérie Wilquet,<sup>1</sup> Denis Belyaev,<sup>3</sup> Anna Fedorova,<sup>3</sup>  
Oleg Korablev,<sup>3</sup> Eric Villard,<sup>4</sup> Franck Montmessin,<sup>4,5</sup> and Jean-Loup Bertaux<sup>4,5</sup>

<sup>1</sup>Belgian Institute for Space Aeronomy, 3 avenue Circulaire, B-1180 Brussels, Belgium

<sup>2</sup>CONSERD, Krekelstraat 27, 9052 Gent, Belgium

<sup>3</sup>Space Research Institute (IKI), 84/32 Profsoyuznaya Strasse, 117997, Moscow, Russia

<sup>4</sup>Service d'Aéronomie du CNRS, BP3, 91371, Verrières-le-Buisson, France; Université Pierre et Marie Curie, Paris, France

<sup>5</sup>Institut Pierre Simon Laplace, Université de Versailles-Saint-Quentin, 78990 Saint Quentin en Yvelines, France

\*Corresponding author: arnaud.mahieux@aeronomie.be

Received 12 November 2007; revised 29 February 2008; accepted 11 March 2008;  
posted 14 March 2008 (Doc. ID 89663); published 25 April 2008

Solar occultation in the infrared, part of the Spectroscopy for Investigation of Characteristics of the Atmosphere of Venus (SPICAV) instrument onboard Venus Express, combines an echelle grating spectrometer with an acousto-optic tunable filter (AOTF). It performs solar occultation measurements in the IR region at high spectral resolution. The wavelength range probed allows a detailed chemical inventory of Venus's atmosphere above the cloud layer, highlighting the vertical distribution of gases. A general description of the instrument and its in-flight performance is given. Different calibrations and data corrections are investigated, in particular the dark current and thermal background, the nonlinearity and pixel-to-pixel variability of the detector, the sensitivity of the instrument, the AOTF properties, and the spectral calibration and resolution. © 2008 Optical Society of America

OCIS codes: 050.1950, 120.0280, 120.6200, 230.1040, 300.6340, 010.1280.

## 1. Introduction

Venus is a very warm (737 K at the mean surface) and dry planet with a dense carbon dioxide (CO<sub>2</sub>) atmosphere. Water is scarcely present and it is not yet known if Venus was already dry at its formation or evolved slowly to its present state. To refine theories and models describing the formation and evolution of Venus and its atmosphere, to characterize the escape of D atoms from the upper atmosphere, and to provide a robust explanation for the problem of the origin of water on Venus, high-resolution vertically resolved measurements of H<sub>2</sub>O and HD, and their

temporal variations, are needed. Information about minor atmospheric constituents, their concentration, reactions, sources, and sinks is also incomplete. In particular, photochemical models of the middle atmosphere would benefit from abundance measurements of NO<sub>x</sub>- and Cl-bearing gases. The SOIR (solar occultation in the infrared) spectrometer is an extension mounted on top of a copy of the SPICAM instrument [1] that currently is flying on Mars Express; the combination is called SPICAV/SOIR [2]. SPICAV/SOIR is one of the seven instruments onboard Venus Express (VEX), a planetary mission of the European Space Agency (ESA) that was launched in November 2005 and sent into orbit around Venus in April 2006 [3].

SOIR [4] is designed to measure at high resolution (0.15 cm<sup>-1</sup>) the atmospheric transmission in the IR

0003-6935/08/132252-14\$15.00/0

© 2008 Optical Society of America

(2.2–4.3  $\mu\text{m}$ ). The solar occultation technique realized by SOIR allows derivation of unique information about the vertical structure and composition of the Venus mesosphere. SOIR is the first high-resolution near-IR spectrometer onboard a spacecraft investigating the Venusian atmosphere, and it enables a sensitive search for new minor species from the top of the clouds up to  $\sim 125$  km of altitude.

The novelty of such a spectrometer and the high accuracy required for determination of minor constituents in the Venusian mesosphere demand precise calibration and an optimized observation process. Most of the important spectrometer calibrations were performed in flight while pointing at the Sun outside the atmosphere. The applied calibration scenario could serve as an example for calibration of similar spectrometers in space. We describe the in-flight performance of SOIR during 1 yr of dedicated solar occultation measurements and the correction and calibration procedure applied to these measurements.

## 2. Instrument Description

The SOIR instrument has already been described in detail [4] and only a short summary will be reported here. SOIR is an innovative, compact, high-resolution spectrometer for remote IR measurements of gaseous species using solar occultations. The system consists of an echelle grating spectrometer (Fig. 1) working in the IR combined with a  $\text{TeO}_2$  acousto-optic tunable filter (AOTF) for the selection of diffraction grating orders. Such an instrument combines the advantages of a high spectral resolution, fast and flexible access to any part of its spectral domain, compactness, and low mass.

The AOTF is a solid-state optical filter that operates by the principle of acousto-optic diffraction in an anisotropic medium. The central wavelength of the filter passband can be rapidly tuned by changing the radio frequency (RF) of the signal applied to the  $\text{TeO}_2$  crystal's transducer. The acoustic wave gen-

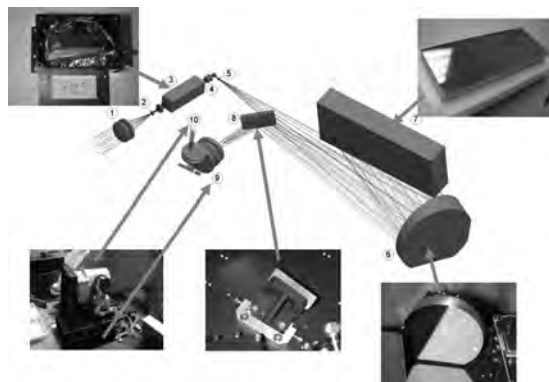


Fig. 1. Optical scheme of the SOIR spectrometer: (1) AOTF entrance optics, (2) diaphragm; (3) AOTF, (4) AOTF exit optics, (5) spectrometer entrance slit, (6) collimating and camera lens merged into one off-axis parabolic mirror, (7) echelle grating, (8) folding mirror, (9) folded detector optics, and (10) detector assembly placed upright.

erated inside the crystal at the transducer modifies the refractive index of the crystal, which, in turn, causes the incident light beam to split into one undiffracted and two diffracted beams, one horizontally polarized and the second one vertically polarized. SOIR uses a noncollinear AOTF. The choice of this geometry has the significant advantage of simpler fabrication procedures. Moreover, the selection of one of the diffracted beams can be done without the use of polarizers. The selected diffracted beam enters the echelle grating spectrometer through the spectrometer entrance slit.

To obtain a compact optical scheme for the high-resolution spectrometer a Littrow configuration was implemented in which the usual collimating and imaging lenses are merged into a single off-axis parabolic mirror, with the additional benefit that no coalignment of two separate lenses is needed. The instrument line profile full width at half-maximum (FWHM) is determined by the slit width and is equivalent to two detector pixels (60  $\mu\text{m}$ ). SOIR is a low power (17 W average) and lightweight instrument (7 kg) that can easily be accommodated onboard planetary missions with tight constraints.

A periscopelike device was added in front of SOIR's entrance aperture because VEX's solar pointing direction is at an angle of  $60^\circ$  with respect to the optical axis of SOIR. As seen from Venus, the solar diameter is 44 arc min, the entrance slit of the spectrometer corresponds to a FOV of  $2 \times 32$  arc min, while one pixel of the two-dimensional (2D) detector corresponds to  $1 \times 1$  arc min. In this spectroimager, the spectrum of each point of the slit is aligned along the lines of the 2D detector, while the slit is aligned with the columns. The detector system is a modified Sofradir integrated detector Dewar cooler assembly, sensitive to radiation in the 1.7 to 4.3  $\mu\text{m}$  spectral region, consisting of a 2D array of photovoltaic HgCdTe pixels (320 columns  $\times$  256 rows) cooled by a Stirling-type cooler (RICOR) to about 88 K.

The choice of the AOTF bandwidth is critical; it should be less than the free spectral range (FSR) of the echelle spectrometer, i.e., the spectral interval in which there is no interference or superposition of light from adjacent orders. Both the AOTF bandwidth and the FSR are measured in terms of FWHM. In the case of SOIR, the FSR equals  $22.38 \text{ cm}^{-1}$  and the bandwidth of the AOTF was originally designed to be  $20 \text{ cm}^{-1}$  [4]. The bandwidth of SOIR measured in flight is  $\sim 24 \text{ cm}^{-1}$ , creating some order leakage overlap on the detector. The wavenumber domain that can be investigated by the SOIR instrument extends from 2256 to  $4369 \text{ cm}^{-1}$  and is divided into 94 smaller ranges corresponding to the different orders (from 101 to 194). The detector width for orders of 101 to 122 is smaller than the FSR of  $22.38 \text{ cm}^{-1}$  and, hence, the detector will lose part of the spectrum. For orders of 123 to 194 the inverse happens; the detector width is equal to or larger than the FSR and the detector will not be completely covered by the selected order.

### 3. Modes of Operation

The SOIR detector has 320 columns along the wavenumber axis and 256 rows along the spatial axis. The slit is projected on 32 fixed rows only (Fig. 2). The constraint imposed by the available telemetry volume means that only a data volume equivalent to eight rows of 320 pixels can be retrieved per second, so one is forced to bin the rows in eight groups of four rows, provided one wants to readout the complete slit and only one order (or AOTF frequency setting) is used during a given second.

However, it is possible to select up to four different orders per second, allowing gathering of a more versatile set of absorption lines. This reduces the maximum measurement time per order to 250 ms and implies that only two larger bins of 16 rows will be used if the complete slit height has to be covered. Other binning factors ( $2 \times 12$  rows,  $4 \times 4$  rows), covering only a limited zone of the slit are also possible. These different binning configurations are illustrated in Fig. 2.

To avoid detector saturation, integration times are set to 20 or 30 ms, depending on the wavelength at which the measurement is taken. To improve the signal-to-noise ratio, a number of measurements can be accumulated as long as the total measuring time remains below 250 ms. One of the advantages of using an AOTF for order selection is that it can be easily used as an electronic background chopper. Each measurement (given integration time and number of accumulations) is immediately followed by an identical measurement with the AOTF switched off. Background measurements are subtracted onboard from the measurements themselves, thereby reducing the time for one measurement to 125 ms maximum, if all four orders are investigated within 1 s. Several observation scenarios have been considered that will be briefly described in Subsections 3.A, 3.B.1, and 3.B.2.

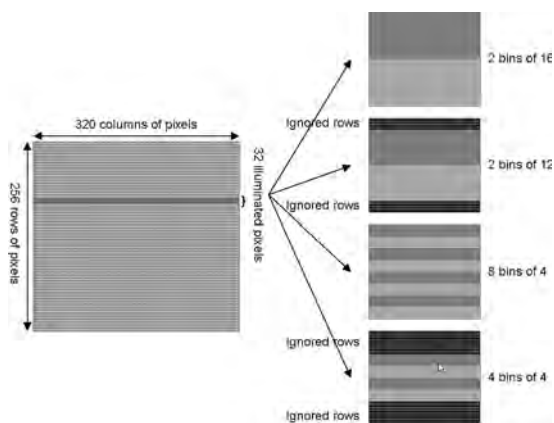


Fig. 2. Detector is an array of  $320 \times 256$  pixels. Because of the dimension of the slit, only 32 rows are illuminated. Several binning configurations have been defined: two bins of 16 rows, two bins of 12 rows, eight bins of four rows, and four bins of four rows.

#### A. Solar Occultation Mode

In the solar occultation mode, SOIR is pointed toward the Sun while the latter sets or rises, allowing probing of different layers of the atmosphere. As a baseline in this mode, four grating orders are scanned each second. In this case, because of the imposed available telemetry volume limits, the data volume produced during each order has to be equivalent to two binned rows. Hence, a binning of two bins of 16 rows is used. Later, binning was changed to two bins of 12 rows (Fig. 2) because the outside rows of the illuminated part of the detector received a lower signal, as that part of the slit was too close to the edge of the Sun.

#### B. Echelle Order Stepping Modes

Two typical calibration modes, called order stepping or scan modes, exploit the ability of the AOTF to quickly select a passband at any place in the spectral domain. In these modes, the AOTF frequency is incremented by a constant programmable value, allowing an AOTF frequency scan from a minimum to a maximum frequency, while all other parameters are kept constant.

##### 1. Miniscan Mode

The minimum and maximum frequencies are chosen to delimit a wavelength interval around one particular spectral feature, e.g., one deep Fraunhofer solar absorption line. This mode allows the precise calibration of the AOTF frequency versus wavenumber and of the AOTF bandpass function. The minimum and maximum frequency, as well as the frequency step, are chosen as a function of the type of measurement; if the goal is to derive the frequency-to-wavenumber relation, the frequency range defined by the minimum and maximum frequencies must cover the frequency corresponding to the wavelength of the spectral feature, and the step must be fine enough to determine unambiguously the frequency corresponding to the signal maximum. If the measurement is aimed at obtaining the AOTF bandpass function, a sufficiently large frequency interval has to be selected to precisely define the intensity of the mainlobes and sidelobes of the function.

##### 2. Full-Scan Mode

In this mode, the minimum and maximum frequencies correspond to the center of SOIR's order 101 ( $12915 \text{ kHz}$  corresponding to  $2266.8 \text{ cm}^{-1}$ ) and 194 ( $26325 \text{ kHz}$  corresponding to  $4354 \text{ cm}^{-1}$ ), respectively, and the frequency increment is chosen such that it matches exactly the FSR ( $145 \text{ kHz}$  corresponding to  $22.4 \text{ cm}^{-1}$ ). This mode of operation allows recording scans over the complete wavelength domain.

#### 4. SOIR Pointing Calibration and Correction

During measurements with SOIR, the spacecraft adopts an inertial pointing mode, meaning that the boresight of SOIR will be pointed, during a pre-

defined period of time, toward a fixed position in the sky. During solar occultation measurements this position is typically a well-chosen point on the solar disk. Any mechanical vector attached to the spacecraft or to the SOIR instrument is defined with respect to a frame fixed to the spacecraft body ( $X$ ,  $Y$ , and  $Z$ ) and by a pair of angles ( $\theta$  and  $\varphi$ ), where  $\varphi$  is the angle of the direction with the plane  $XY$  and  $\theta$  is the angle of the projection of the direction on the  $XY$  plane with the  $X$  axis. In particular, the boresight of SOIR is defined by nominal values  $\theta = 30^\circ$  and  $\varphi = 0^\circ$ . An inertial pointing is commanded by asking the spacecraft to orient itself so that a given celestial direction (i.e., a given point on the solar disk, determined by right ascension and declination) coincides with the desired instrument direction, i.e., the boresight.

Because of mechanical misalignment, the actual position of the SOIR boresight is not exactly the nominal one. Since this misalignment was not well measured before launch, it was calibrated during a sequence of measurements using the solar disk as a pointing target, placed at various positions ( $\theta$  and  $\varphi$ ) in the frame of the spacecraft. To correct for the pointing misalignment, first a raster of nine points, with an angular spread of 30 arc min in both the  $\theta$  and  $\varphi$  directions and centered around the nominal position of the boresight ( $\theta = 30^\circ$  and  $\varphi = 0^\circ$ ), was scanned. Looking at the position of the Sun and the change in intensity in the SOIR slit for these nine points, a first approximation for the deviation between the SOIR boresight and the satellite pointing direction was derived. In consecutive pointing tests, similar measurements were done with a finer grid (5 arc min) leading to a precise measurement of the misalignment ( $\theta = 29^\circ 44$  arc min and  $\varphi = 0^\circ 04$  arc min).

The atmosphere of Venus is very dense, hence, at an altitude of 65 km the air pressure already is as high ( $\sim 73$  mbars) as at an altitude of 18 km on Earth. At the altitude of 49.5 km the pressure reaches the same value as on the Earth's surface. This means that refraction should be taken into account for a precise pointing.

To account for the change in apparent height of the Sun in Venus's atmosphere and the flattening of the solar disk due to atmospheric refraction effects during sunset and sunrise, a constant offset of +10 arc min is added to the SOIR boresight, meaning that a point on the solar disk is targeted 10 arc min above the solar center (away from the planetary limb). The value of the offset was estimated using the Magellan mission data ([http://atmos.nmsu.edu/PDS/data/mg\\_2401/](http://atmos.nmsu.edu/PDS/data/mg_2401/), orbit 3212) for the air refraction coefficient. The use of progressive pointing adjustment (e.g., variable offset) would take into account even more accurately the effect of diffraction of the sunlight, and hence, enhance the performance of the instrument at low altitudes.

To estimate the fraction of the solar disk covered by SOIR's field of view, the position of the slit on

the solar disk was calculated. The result for one particular observation (orbit 209) is presented in Fig. 3. The solar disk position was modeled with (bold ellipses and a dotted line) and without (dashed line) taking the refraction into account. The modeling shows that the slit stays within the solar disk until the boresight's tangent height reaches an altitude of  $\sim 60$  km and quickly leaves the solar disk at lower altitudes.

Defining a pointing direction by putting a celestial direction ( $\alpha, \delta$ ) at a given angular position ( $\theta, \varphi$ ) in the frame of the spacecraft allows  $1^\circ$  of freedom for the spacecraft orientation about the pointing direction. Spacecraft orientation is fully defined with the additional requirement that the projection of the SOIR slit becomes parallel to the Venus limb at a geometric tangential height of  $\sim 65$  km. At other tangential heights, the slit will have a small inclination angle with respect to the limb, degrading slightly the vertical resolution. This will also have some effect on the retrievals because of the change in pressure broadening of the molecular absorption lines, their temperature dependence, and the difference in ray path. This is outside the scope of this paper and will be further discussed in a forthcoming paper [5]. This inclination angle, as well as all parameters defining the geometry, are given in ESA's archive, as it varies from one orbit to another.

## 5. In-Flight Spectral Performance and Calibration Measurements

Raw spectra registered by SOIR and transmitted to Earth need dedicated processing in order to upgrade them to a calibrated data set. A number of instrumental parameters have to be characterized in flight in order to be able to calibrate and correct the spectra. In-flight characterization is necessary since some instrumental parameters were not measured before take off, but also because they might have changed since launch, or might change during the op-

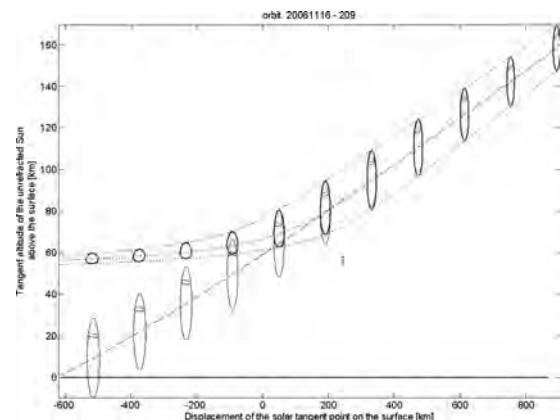


Fig. 3. Modeled view of solar occultation measurements (orbit 209) with (bold ellipses and dotted line) and without (dashed line) refraction. The position of the slit on the solar disk is indicated by a rectangle. The coordinates are the tangent altitude of the unrefracted Sun and the horizontal displacement of the solar tangent point from the point where the slit is parallel to the limb.

erational life of the instrument. One noticeable change concerns the response of the AOTF; it originally was designed to be compatible with the free spectral range of the echelle spectrometer, but it proved to have a slightly broader bandwidth after environmental testing. A thorough in-flight calibration is therefore necessary.

Below the different steps that are taken in the correction and calibration procedure of the SOIR spectra are summarized and then discussed in more detail:

- Thermal and dark current (see Subsection 5.A) is measured and subtracted onboard.
- Detector nonlinearity correction (see Subsection 5.A): the detector response to incident light is not linear over the complete dynamic range of the well capacity. For low signals, a nonlinearity correction has to be applied.
- Bad pixel and pixel-to-pixel variability correction (see Subsection 5.B): the properties, i.e., the gain, of each pixel differ slightly. Moreover, some (bins of) pixels show an unpredictable or systematically wrong behavior. Their values are removed and replaced by values of adjacent pixels or bins.
- Sensitivity correction (see Subsection 5.C) takes into account the nonconstant overall instrument sensitivity as a function of wavelength.
- AOTF frequency-to-wavenumber calibration, also called tuning relation (see Subsection 5.D): establishing an AOTF tuning relationship between the applied RF and the selected wavenumber domain and bandpass curve.
- Spectral calibration, which transforms pixel number into wavenumber and evaluates the calibration error (see Subsection 5.E).
- Signal-to-noise ratio (see Subsection 5.G).
- Division by a reference solar spectrum: ideally the reference spectrum that is taken outside the atmosphere would be measured with an identical relative slit position with respect to the solar disk. Attitude drift of the spacecraft makes the slit float. However, it results in a gradual linear change of the intensity. This effect is corrected for (see Section 6).

Finally, the spectral resolution of the instrument has also been derived from in-flight measurements and its evolution over the entire spectral domain has been investigated (see Subsection 5.F).

#### A. Thermal Background, Detector Dark Current, and Nonlinearity Corrections

Before the start of the measurement, the detector is cooled to a temperature of 88 K. This precooling lasts for 600 s. Thermal background and detector dark current are directly subtracted from the measurements onboard. In fact, as already mentioned, one spectrum is the subtraction of two recordings performed one after the other; the first recording is taken with the AOTF on and corresponds to the num-

ber of signal photons  $S$  plus the number of background photons  $B(S+B)$ . The second recording with AOTF off corresponds to the background only ( $B$ ) and contains a contribution of the detector dark current and the thermal emission of the optics between the AOTF and the detector. Signals  $S$  and  $S+B$  are obtained onboard after digitization of the analog output of the detector, and usually only the digital difference  $(S+B) - B$  is transmitted to ground.

The AOTF state is supposed to remain constant between the measurements of  $S+B$  and  $B$ . The AOTF temperature is assumed to remain constant as the AOTF is only on for 20 ms. The crystal characteristics remain the same during the measurement of  $S+B$  and  $B$ , and the surface, perpendicular to the light path, does not change, either. So, background signal would depend only on temperature, which is constant, and constantly measured onboard.

For the low signal intensities (below 25% of the full well capacity) the detector has a nonlinear response [6]. It is important to correct for this behavior to not distort the ratios between weak and stronger absorption lines. Both absorption spectra (AOTF on) and background spectra (AOTF off) should be subject to this correction. However, since onboard background subtraction  $((S+B) - B)$  is applied, spectra containing only the signal contribution  $S$  are available on ground. Therefore, an approximate method for nonlinearity correction has to be used (Fig. 4). During observation sessions of the dark sky a so-called linearity plot is constituted, giving the thermal background plus the detector dark signal ( $B$ ) as a function of integration time.

The linearity plot in Fig. 4 (21 February 2006) confirms the nonlinear behavior for low collected pixel charge. The pixel charge is converted by the detector read-out process into analog-to-digital converter (ADC) units. In Fig. 4 the ADC units have been scaled to correspond to one accumulation and one pixel. With measurement 1 ( $S+B$ ) and measurement 2 ( $B$ ) ADC values  $ADC_{S+B}$  and  $ADC_B$  corre-

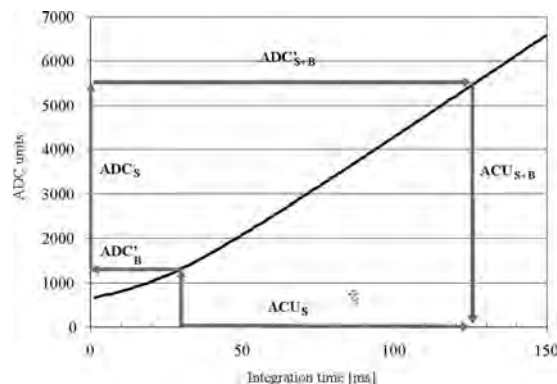


Fig. 4. Method for detector nonlinearity correction.  $ADC_S$ : ADC is the value available on ground,  $ADC'_{S+B}$  and  $ADC'_B$  are approximation of codes for signal plus background and background, and  $ACU_{S+B}$ ,  $ACU_B$ , and  $ACU_S$  are the total, signal, and background pixel charge in arbitrary units.

spond. Only the subtraction of these ADC values  $ADC_S = ADC_{S+B} - ADC_B$  is available on ground.

It is assumed that the linearity plot provides a good approximation ( $ADC'_B$ ) for  $ADC_B$  at the given integration time of a spectrum and for the instrument temperature at the time of the measurement. Then the total signal  $S + B$  before subtraction can be estimated by adding  $ADC'_B$  to the transmitted ADC value  $ADC_S$ :  $ADC_{S+B} \approx ADC'_{S+B} = ADC_S + ADC'_B$ .

Since the linearity plot does not give the relation between the physical number of electrons or charge on a pixel and the recorded ADC value (no calibration has been performed), the notion of arbitrary charge units (ACU) is introduced; the integration time (in ms) at which a code  $ADC'_B$  is registered is taken as the (arbitrary) charge accumulated on the pixel. The relation between ADC and ACU can be approximated by a polynomial of degree 10 for ADC values below 6000, and by a linear function for ADC values above 6000. Now the number of photons  $S + B$  and  $B$  can be expressed as  $ACU_{S+B}$  and  $ACU_B$  ( $ACU_B$  is nothing other than the integration time in milliseconds), and the number of photons that can be attributed to the signal  $S$  (pure signal, no background), corrected for nonlinear detector effects, is  $ACU_S = ACU_{S+B} - ACU_B$  (Fig. 4). The detector residual error was measured when no light was passing through the optics. The standard deviation is about 0.2 ADC units.

### B. Pixel-to-Pixel Nonuniformity

Flat-field correction takes into account the difference in quantum efficiency of the detector pixels. For solar occultation observations these differences can be canceled out by taking a solar reference spectrum outside Venus's atmosphere under the same conditions and then dividing each atmospheric absorption spectrum by this reference spectrum. Note that this will not apply for measurements used for the determination of the AOTF bandpass function, where raw data are used without division by a reference spectrum.

The pixel-to-pixel nonuniformity is an intrinsic characteristic of the detector. It originates from the fact that the physical properties of each pixel of the detector differ slightly. In the laboratory, pixel-to-pixel nonuniformity is measured by illuminating the detector directly, without passing through the spectrometer, with a homogeneous light source. By repeating this measurement several times and with different exposure times, the influence of the latter is removed and random noise is reduced. After removing the continuous component of these spectra, the pixel-to-pixel nonuniformity is obtained. This correction has to be applied to the raw signal recorded during a real measurement and will compensate for the different gains from pixel to pixel. This function needs to be monitored in time, as aging of the detector can induce variations of the pixel response.

However, for SOIR, due to the very tight instrument development and test schedule, these measure-

ments could not be performed before launch. We will show that it is possible to extract useful information from the solar spectra obtained in flight by SOIR. Solar spectra recorded in the full-scan mode outside the Venus atmosphere were considered. Several orders were selected that correspond to spectral regions where no or only very weak solar lines are present ( $<0.03\%$  of transmittance). A high number of spectra corresponding to the same order were used to statistically reduce random noise. High-pass filtering of those spectra removes the general response curve of the AOTF, the optics and the spectrometer, leaving only the pixel-to-pixel nonuniformity. Figure 5 illustrates the method used for determining the pixel-to-pixel nonuniformity.

As by definition this nonuniformity depends on the physical pixel and on the chosen binning, one must construct flat-field correction functions for every binning mode used by SOIR. In particular, in the solar occultation mode using a binning of  $2 \times 12$  rows or  $2 \times 16$  rows, the pixel-to-pixel nonuniformity will differ for the bin 1 and bin 2 spectra.

### C. Spectral Sensitivity Curve

The spectral sensitivity curve describes the dependence of the SOIR instrument as a function of the wavelength of the incoming light. Because this wavelength was selected through the AOTF, the spectral sensitivity may be expressed in terms of AOTF frequency, after the pixel-to-pixel variation has been removed from the spectra. An important contribution to the irregular form of the sensitivity curve comes from the AOTF diffraction efficiency dependence on wavelength and the imperfect matching of the RF driver output impedance to the AOTF transducer impedance.

The spectral sensitivity curve was obtained from direct Sun observations, with a binning of eight groups of four pixel rows in the spatial direction, while SOIR is in full-scan mode (see Subsection 3. B.2). This is shown in Fig. 6. Groups of 10 pixels were

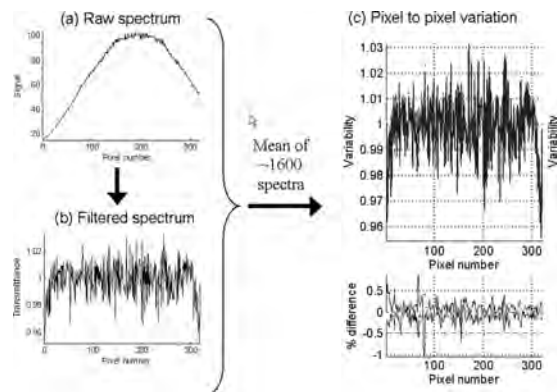


Fig. 5. Pixel-to-pixel nonuniformity: (a) a spectrum where weak solar lines are present is selected, (b) high-pass filtering is applied, and (c) other spectra where weak solar lines are present are selected and filtered ( $\sim 1600$  in total), then the global average is calculated (top panel). The percentage difference relative to the mean is shown in the bottom panel.

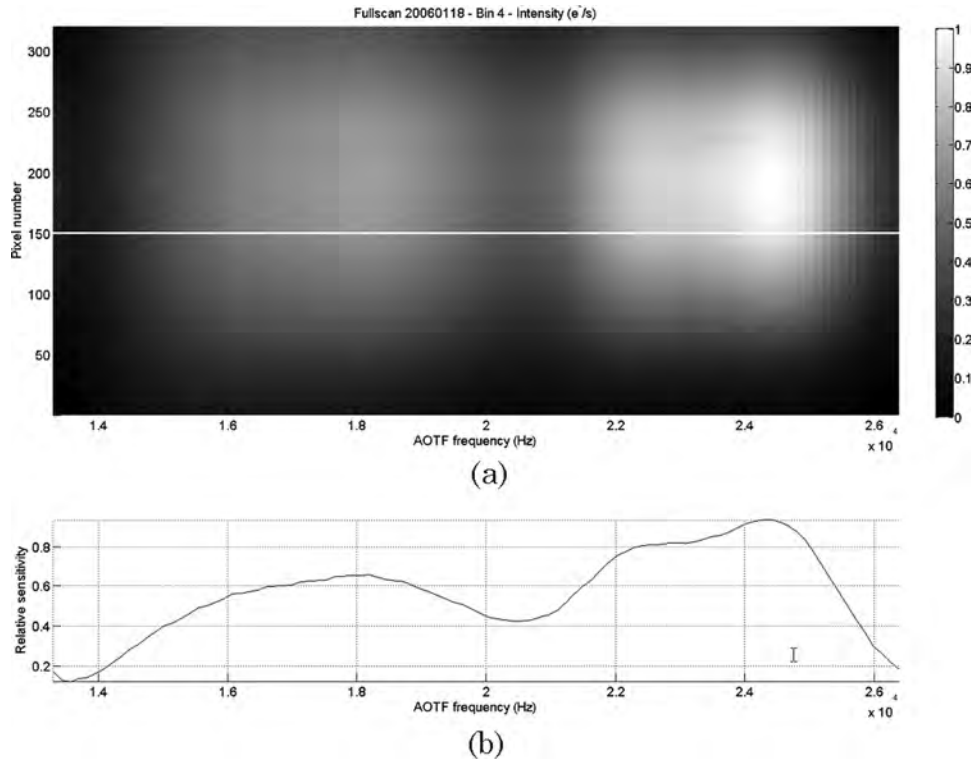


Fig. 6. Overall sensitivity of the SOIR instrument: (a) sensitivity of bin 4 of the detector in a binning case of eight bins of four rows and (b) sensitivity of row 150 with respect to the AOTF frequency. This row is highlighted in the top figure.

considered in the spectral direction to smooth out the contribution of unavoidable solar absorption lines. Linear interpolation was performed afterward to recover the spectral sensitivity curve for all pixel rows. The spectral sensitivity curve should be monitored over time as it reflects the intrinsic behavior of the instrument and may slightly change during SOIR's life. Based on the sensitivity curve, optimized integration times were determined for each recording condition.

The sensitivity of the instrument should be taken into account when analyzing raw data. The effect of wavelength dependent instrument sensitivity cancels itself out, however, when transmittances (i.e., ratios of two spectra obtained under similar conditions) are calculated. The sensitivity curve determines the signal-to-noise ratio for different spectral ranges of the instrument and the error level for the retrieval of different gaseous constituents.

#### D. Filter Tuning Relation and Bandpass Response

At a fixed radio frequency  $f$ , the AOTF selects only a narrow wavelength band. The central wavelength  $\lambda$  of a given band is determined by the momentum matching condition and can be estimated by the following expression [7], also called the tuning relation of the AOTF:

$$f = \frac{v\Delta n}{\lambda} (\sin^4\theta_i + \sin^2 2\theta_i)^{1/2}, \quad (1)$$

where  $\theta_i$  is the incident angle,  $v$  is the acoustic velocity, and  $\Delta n$  is the birefringence of the crystal. The

tuning function follows approximately a  $1/\lambda$  law, but not exactly because of the wavelength dependence of the refractive indices. The refractive indices of  $\text{TeO}_2$  have been measured by Uchida [8], and the dependence of the birefringence on wavelength has been shown to follow the simple approximation formula [9]

$$\Delta n = \frac{a}{\lambda - \lambda_c} + b, \quad (2)$$

where  $a$ ,  $b$ , and  $\lambda_c$  are constants ( $a = 7.156$  nm,  $b = 0.1338$ , and  $\lambda_c = 262.9$  nm for  $\text{TeO}_2$ ).

The intrinsic passband of an AOTF is determined by the effect of momentum mismatch caused by the deviation of wavelength from the exact wave vector momentum matching condition in the filter transmission [7]. The transmission of an AOTF can be written as

$$T = T_0 \text{sinc}^2 \left( 0.886 \frac{\lambda - \lambda_0}{\Delta\lambda_{\text{FWHM}}} \right), \quad (3)$$

where  $\lambda_0$  is the peak wavelength,  $T_0$  is the peak transmission,  $\text{sinc}(x) = \sin(\Delta x)/\Delta x$ , and  $\Delta\lambda_{\text{FWHM}}$  is the bandpass FWHM, which can be approximated [7] by

$$\Delta\lambda_{\text{FWHM}} = \frac{1.8\pi\lambda_0^2}{b_\lambda L \sin^2\theta_i}, \quad (4)$$

where  $L$  is the acoustic interaction length in the crystal

$$L = \frac{W}{\cos(\theta_i - \alpha)}, \quad (5)$$

with  $W$  as the transducer width (36 mm) and  $\alpha$  as the angle of incidence of the acoustic wave ( $9^\circ 10'$ ), and  $b_\lambda$  is the dispersive constant

$$b_\lambda = 2\pi \left( \Delta n - \lambda \frac{\partial \Delta n}{\partial \lambda} \right) = 2\pi \left( \Delta n + \frac{\lambda \cdot a}{(\lambda - \lambda_c)^2} \right), \quad (6)$$

where  $a$  and  $\lambda_c$  are the parameters already defined in Eq. (2). Equation (4) can be rewritten in terms of wavenumber

$$\Delta\nu_{\text{FWHM}} = \frac{1.8\pi}{b_\lambda L \sin^2 \theta_i}, \quad (7)$$

which indicates that the FWHM bandpass is essentially constant when expressed in wavenumber if the dependence of  $b_\lambda$  on wavelength is neglected.

In addition, the passband is broadened by several other effects, such as the divergence of the incident optical beam, the angular spread of the acoustic beam, and the optical nonuniformity of the acousto-optic material. In fact, here we will demonstrate that the AOTF transmission in SOIR, in particular its width and peak position, is different for each of the pixel bins on the detector. In the normal mode of observation used for solar occultation measurements two spectra are recorded simultaneously, corresponding to two super bins of 16 detector lines, further defined as bin 1 (detector lines 188 to 203) and bin 2 (detector lines 204 to 219) spectrum (see Fig. 2). For both bin 1 and bin 2 spectra, a tuning function and AOTF bandpass functions have to be determined, as Eq. (4) shows that the width of the AOTF bandpass function depends on wavelength. Modeling these bandpass functions as a function of wavelength allows us to refine the wavelength-to-frequency relation.

Miniscan observations have been dedicated to the determination of the AOTF bandpass function. Each miniscan was centered on an AOTF frequency corresponding to a well-defined solar line. This solar line will be observed on a precise pixel. Other solar lines from the neighborhood of the targeted one are often also visible on other pixels, which allows retrieval of many more AOTF bandpass functions at the same time. The study of the variation of the measured intensity as a function of the applied frequency allows the precise characterization of the bandpass function. The determination of the wavelength-to-frequency relation has been performed using the same miniscan observations and by determining the position of the function maximum.

Assuming that  $f$  is the AOTF frequency that corresponds to the wavelength of the solar line, two types of miniscan observation were defined and performed:

- from  $f - 500$  kHz to  $f + 500$  kHz in steps of 20 kHz, and later another type has been used, and
- from  $f - 225$  kHz to  $f + 225$  kHz in steps of 15 kHz.

The correction procedure first handles the pixel-to-pixel nonuniformity (Subsection 5.B) and the sensitivity of the instrument (Subsection 5.C). On top of that, spectra are flattened using a baseline level; since the observed solar line is recorded on one pixel only, the levels in the adjacent pixels can act as reference level for base level subtraction. The residual base level has been fitted as a second order polynomial. Figure 7 illustrates the method applied to derive the AOTF bandpass function using the solar line at  $2943.69 \text{ cm}^{-1}$ .

The same procedure has been applied to all available miniscans (42 in total). Figure 8 shows the results obtained for three typical solar lines. The retrieval has been done using about 250 solar lines widespread along the spectrum, for all bins and binning cases. They all show a transmittance deeper than 0.88. The shape of the bandpass does not show high variation over the entire SOIR spectral domain, as shown in Fig. 8, where the curves correspond to cardinal sine functions

$$I(\nu) = I \cdot \left[ \text{sinc} \left( 0.886 \cdot \frac{\nu - \nu_0}{\Delta\nu_0} \right) \right]^2, \quad (8)$$

where  $I$ ,  $\nu_0$ , and  $\Delta\nu_0$ , are parameters whose values are obtained by best fitting this expression to the observed AOTF bandpass functions, while fitting the baseline level by a second order polynomial function. Using such an approximation, an AOTF bandpass

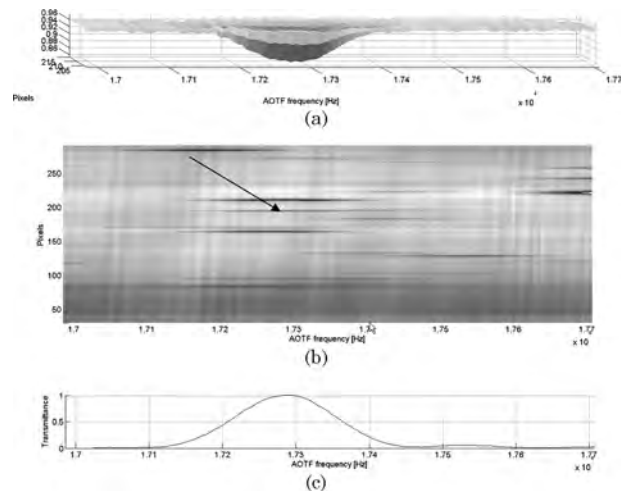


Fig. 7. Measured AOTF bandpass functions at  $2943.69 \text{ cm}^{-1}$  (binning  $4 \times 8$ ): (a) presents the measurements of the intensity (bin 4 on the detector) versus the AOTF frequency and the pixel number after correction for the pixel-to-pixel variability and instrument sensitivity, showing the residual background level, (b) is obtained when this background is removed from the measurements, and (c) shows the AOTF bandpass corresponding to the  $2943.69 \text{ cm}^{-1}$  solar line.

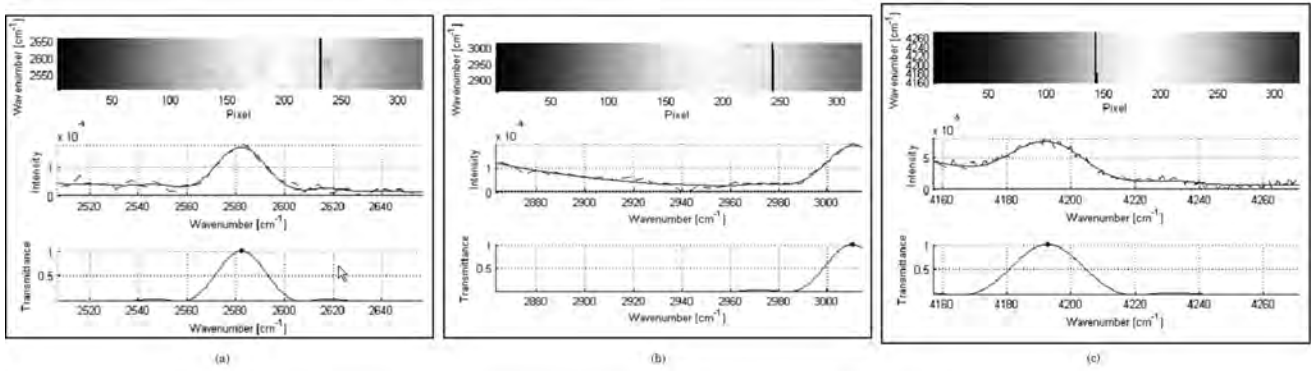


Fig. 8. AOTF bandpass functions for a binning of 12 for bin 1 by analyzing the solar lines situated at (a)  $2583.79\text{ cm}^{-1}$ , (b)  $3012.03\text{ cm}^{-1}$ , and (c)  $4193.03\text{ cm}^{-1}$ . Top panel of each figure shows the measured value on the detector with respect to the AOTF frequency. Concerned pixel line is highlighted. Middle panel shows the measured bandpass function (dashed) and fitted function (plain). Bottom panel shows the retrieved AOTF bandpass function.

function can be derived at any given wavenumber of the investigated spectral range.

Figure 9 shows the evolution of the FWHM of the AOTF bandpass throughout the entire spectral domain. These values have been obtained by considering the different bandpass functions for the 250 solar

lines. The top of Fig. 9 describes the FWHM for bin 1, and the bottom for bin 2 (in a  $2 \times 12$  binning case). Error bars, which were returned by the fitting algorithm, were used as weighting factors for determining the FWHM. Table 1 gives the value of the FWHM, which should be compared to the theoretical

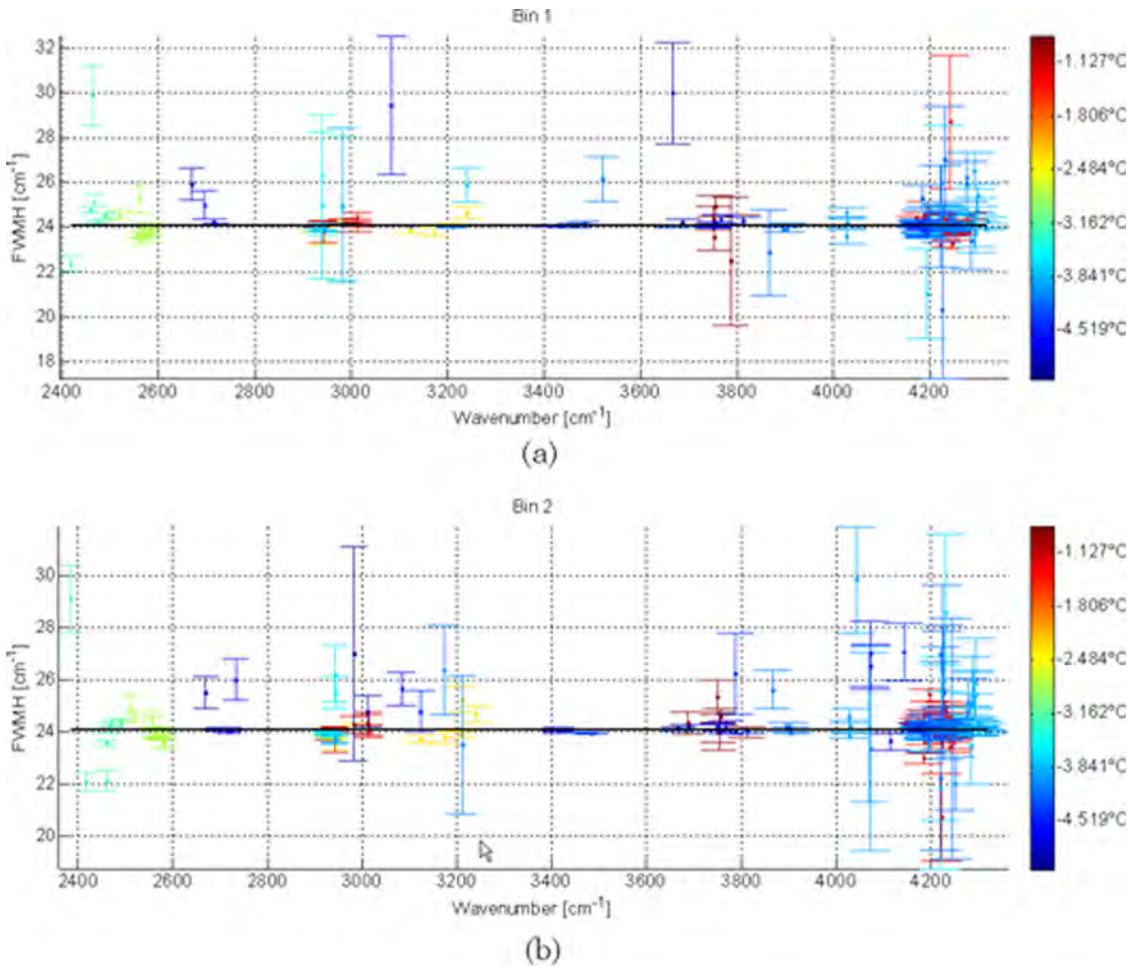


Fig. 9. (Color online) Evaluation of the FWHM of the passband function using the dedicated miniscan: (a) bin 1 and (b) bin 2. In both panels, color indicates temperature of the AOTF at the time of measurement of the maximum of the bandpass function.

Table 1. Coefficients for the Wavenumber-to-Frequency Relation (Tuning Function) for Bins 1 and 2<sup>a</sup>

Binning Case	Bin Number	Tuning Function			FWHM
		A	B	C	
2 × 12	1	1.8914633080e-7	0.14774334848	336.08036871	24.145852651
2 × 12	2	1.9604792544e-7	0.14711671129	338.40229096	24.118470220
2 × 16	1	1.7571424024e-7	0.14835498551	330.01948237	24.182093372
2 × 16	2	1.9483230511e-7	0.14707548060	338.89075713	24.099412078

<sup>a</sup>Frequency in kHz, wavenumber in cm<sup>-1</sup>, and value of the FWHM of the AOTF bandpass function in cm<sup>-1</sup>.

value of 18.0 cm<sup>-1</sup> derived from Eq. (7), and the design value of 20 cm<sup>-1</sup> [4]. The difference among theory, design, and reality is explained by degradation of the crystal quality after overstressing during environmental testing before launch (both thermal and mechanical).

The determination of the position of the maximum of the AOTF bandpass function allows derivation of the wavenumber-to-frequency relation (tuning function). This is illustrated in Fig. 10, where the tuning function is plotted for bin 1 and bin 2 of a 2 × 12 pixel row configuration. The frequency steps of each min-

iscan measurement were used as weighting factors. The tuning function can be fitted by a second order polynomial linking the radio frequency (*f*) in kHz to the wavenumber (*ν*) in cm<sup>-1</sup> by

$$\nu = a \cdot f^2 + b \cdot f + c, \quad (9)$$

where *a*, *b*, and *c* are given in Table 1 for bins 1 and 2 in the configurations of 2 × 12 pixel rows and 2 × 16 pixel rows. This function describes the position of the maximum of the AOTF bandpass function versus wavenumber and is important, because only a small

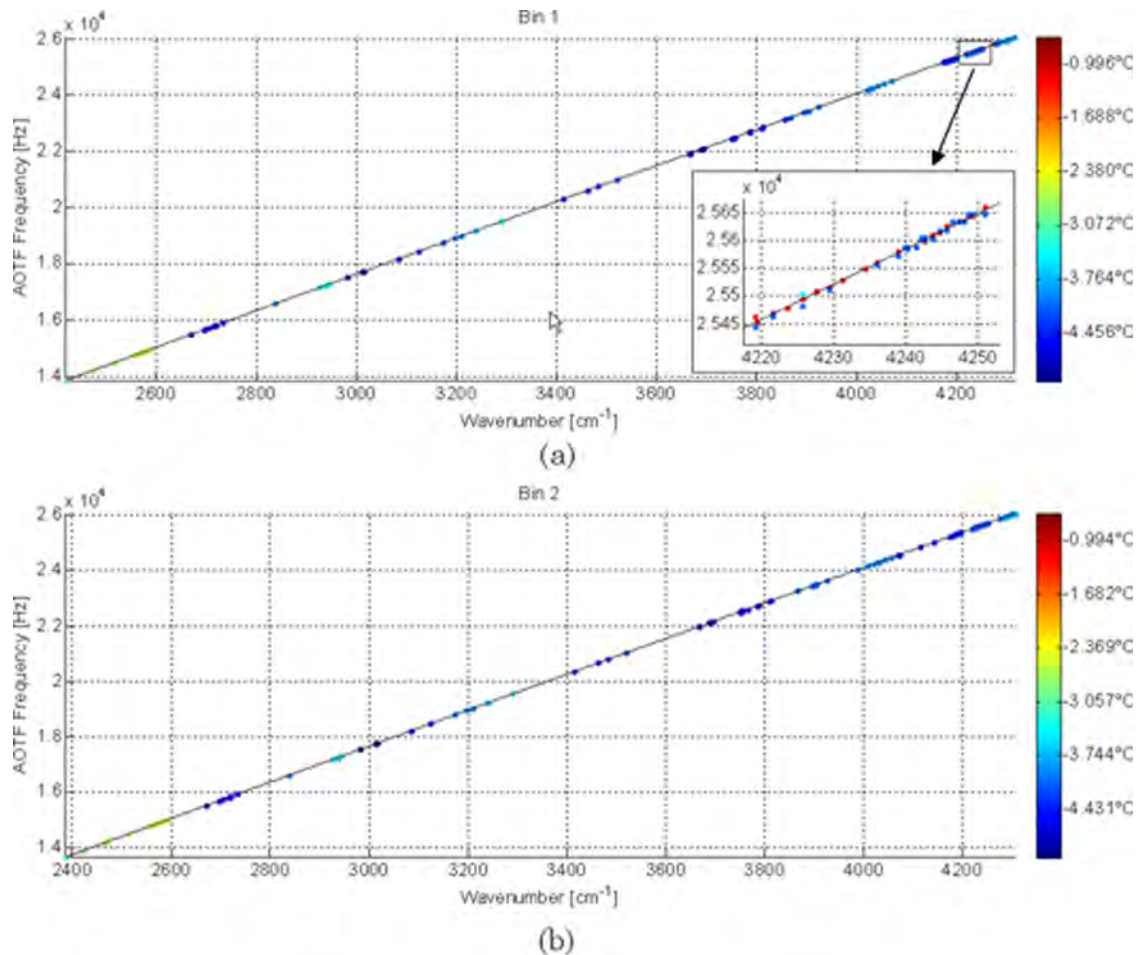


Fig. 10. (Color online) Tuning relations for bins 1 and 2 of the detector: (a) wavenumber-frequency relation for bin 1 derived from miniscans measurements; a zoom on the right side of the fit is included; and (b) wavenumber-frequency relation for bin 2 derived from miniscans measurements. In both panels, color indicates temperature of the AOTF at the time of measurement of the maximum of the bandpass function.

shift of the bandpass can introduce large deformations in the transmitted spectrum. The error on the function has also been calculated. For a binning equal to 12 and for bin 1, the mean value of the error is  $0.83 \text{ cm}^{-1}$ . In Figs. 9 and 10, the color of the points represents the AOTF temperature at the time of measurement, only covering a range of  $3^\circ$ . From these figures no detectable temperature dependency was observed either for the tuning function or for FWHM, the variation being within the error bars.

As mentioned in Section 2, the AOTF bandwidth is larger than the FSR, which introduces order overlapping. To account for this effect during a profile inversion, adjacent orders of diffraction must also be studied. A tabulation of the contribution of adjacent orders is given in the first three rows of Table 2, for a central order equal to 148. The second row shows the maximum value reached by the AOTF transfer function within the order, while the third row shows the average contribution of the order to the total signal. By considering the three first adjacent orders, 96.78% of the contribution is taken into account.

If the AOTF transfer function is not perfectly centered on the central order, it will induce variations in the contributions of the orders. It is tabulated in the two last rows of Table 2 for a shift equal to the mean error on the AOTF transfer function determination. The first adjacent orders will see their contribution vary slightly (about 2%), while the central order will vary by about 0.1%. Order overlapping and transmittance calculation are extensively described in a forthcoming paper [5].

#### E. Spectral Calibration (Wavenumber-Pixel Calibration)

The pixel-to-wavenumber relation has been obtained by analyzing well-defined solar lines in the full scan measurements outside the atmosphere. Such measurements are performed regularly to follow the evolution of the spectral calibration in time, as well as the aging of the instrument. The spectral calibration results from the fitting of a polynomial relation between the wavenumber positions of about 100 solar lines and the pixel position of the observed lines. Those lines are observed in different orders to cover the full wavenumber range. Different polynomial fits up to order 5 have been tested. The average error in pixel position on the selected solar lines was studied as a function of the order of the polynomial used for

the pixel number-wavenumber calibration. It turned out that a linear calibration relation is not sufficient and that above order 3 no real improvement is obtained, so a polynomial of order 3 has been chosen for this calibration. The average error on the pixel position is about 0.57 pixels.

The spectral error was computed by comparing full Sun raw spectra taken by SOIR with tables listing the known solar absorption lines [10]. The peak position of about 30 solar lines was compared throughout the entire scanned range, and position differences were computed. Because different binning cases have been used ( $2 \times 12$  pixel rows and  $2 \times 16$  pixel rows, see Section 3.B.1), this spectral error has been computed for all bins of all binning configurations. The error is constant ( $0.05 \text{ cm}^{-1}$ ) over the whole detector width; no pixel number dependency has been observed.

#### F. Spectral Resolution

Two fundamental parameters defining the performance of a spectrometer are its spectral sampling interval (SSI) and its instrument line profile (ILP). Based on the theoretical optical design the SSI was predicted to have a value of  $0.1 \text{ cm}^{-1}$  per pixel and an ILP with a FWHM of  $0.2 \text{ cm}^{-1}$ . Before flight both characteristics were verified using a He-Ne laser line at  $3.39 \mu\text{m}$  and in a rudimentary test with the Sun as a source. Although these tests confirmed the order of magnitude of both SSI and ILP, they are valid only in a very limited part of the spectral domain. No systematic spectral resolution performance tests over the entire domain could be carried out before launch.

Therefore, during flight more detailed resolution measurements were performed, making use of solar absorption lines in spectral recordings outside the atmosphere. The ILP of SOIR was approximated by a sinc square function whose width was determined by comparing well-defined and relatively well-isolated solar lines. The selected spectra corresponded to altitudes above 280 km where absorption by  $\text{CO}_2$  does not yet influence the solar spectrum. The selected spectra were first corrected for the pixel-to-pixel non-uniformity and instrument sensitivity variations.

In the simulation, a high-resolution solar spectrum [10] is multiplied by the appropriate AOTF function, the contributions of seven adjacent orders

Table 2. Adjacent Orders Contribution from the AOTF Transfer Function for a Central Order Equal to 148<sup>a</sup>

Order		143	144	145	146	147	148	149	150	151	152	153
AOTF centered	Maximum value (%)	0.74	0.83	1.65	4.72	77.82	100	69.43	4.72	1.65	0.83	0.69
	Mean value (%)	0.24	0.35	0.65	1.85	16.20	62.32	13.28	1.84	0.65	0.35	0.26
AOTF shifted	Maximum value (%)	0.83	1.22	1.65	4.72	92.60	100	49.27	4.72	1.65	0.83	0.50
	Mean value (%)	0.27	0.40	0.69	1.86	24.04	59.72	8.09	1.70	0.66	0.33	0.22

<sup>a</sup>First row is the order, the next two rows are for the AOTF transfer function centered in the central order, and the last two rows are for the AOTF transfer function shifted by  $0.83 \text{ cm}^{-1}$ . For both cases, the first row is the maximum contribution in terms of transmittance within the order in percent. The second row is the mean contribution of the order, normalized by the total AOTF contribution of all orders (101 to 194).

are coadded, and finally, the spectrum is convolved with a sinc square function. The FWHM of the sinc square is tuned until the best agreement is found between the observed line and the simulation. A result of such a comparison is shown in Fig. 11. Using a series of solar lines in different grating orders, the evolution of the ILP could be obtained for the entire spectral domain and is presented in Fig. 12. It is shown that the ILP varies from 0.07 to 0.22 cm<sup>-1</sup> across the entire spectral interval.

### G. Signal-to-Noise Ratio

The signal-to-noise ratio has been calculated for all recorded spectra using

$$\frac{S}{N} = \frac{1}{\frac{1}{\sqrt{P_x \cdot n_x}} + \frac{1}{\nu_y \cdot \sqrt{P_y \cdot n_y}}}, \quad (10)$$

where S is the signal, N is the noise, subscripts *x* refer to spectra taken in the atmosphere, *y* refers to reference spectra (full Sun spectra outside the atmosphere), *P* stands for the number of photons reaching the detector, *n* is the number of accumulations, and  $\nu$  is the number of points used for the regression of the full Sun spectra (see Section 6 and forthcoming paper [5]). The values of the signal-to-noise ratio calculated from the raw spectra (before dividing by spectra taken outside the atmosphere) were found to be between 500 and 650 in general, depending on the signal level.

## 6. Measurements

A SOIR occultation observation can be taken either at sunset or sunrise. The following case study is for a sunset, but sunrises can be treated similarly; only altitudes of observation will increase with time. Well before the instrument's line of sight to the Sun intersects with the top layers of the atmosphere, the measurement cycle is started and reference spectra are recorded (at a rate of one spectrum per second). Once

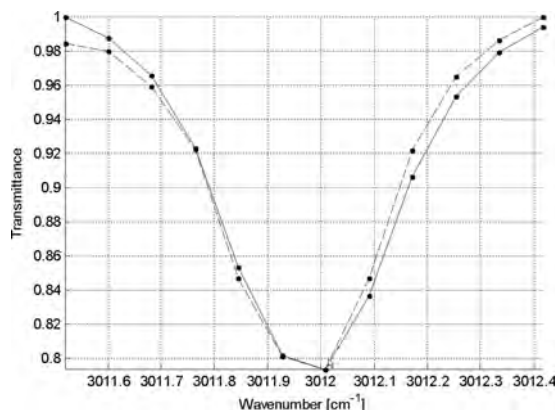


Fig. 11. Determination of the spectral resolution of the SOIR instrument. The observed solar line at 3012.96 cm<sup>-1</sup> (dashed curve) measured in order 134, during orbit 227 and the fitted line (solid curve) are compared. The latter was obtained by convoluting a high-resolution solar spectrum with a sinc square function of 0.149 cm<sup>-1</sup> FWHM.

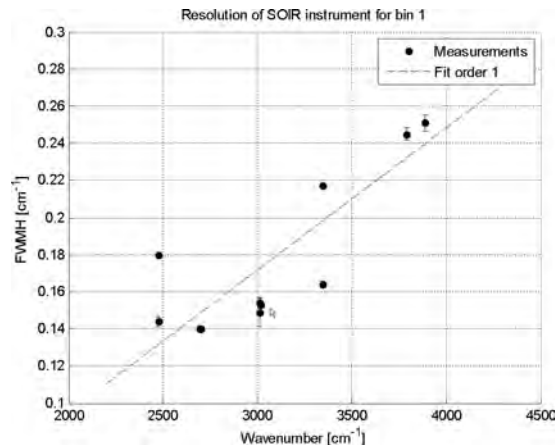


Fig. 12. Evolution of the observed FWHM of the instrumental line profile throughout the spectral domain.

the top of the atmosphere is reached, solar light is absorbed and the intensity of the recorded signal starts to decrease until the Sun gets so flattened that the spectrometer slit moves out of the diffracted solar disk (see Section 4). The altitude is retrieved from the spacecraft attitude and orbital data provided by the European Space Operations Centre.

Figure 13 illustrates the signal intensity measured during a typical occultation. As one can see, the direct solar intensity observed before the occultation is not constant. This is due to a drift of the satellite during the measurement, resulting in a slight apparent motion of the slit over the solar disk.

One of the main advantages of solar occultations is that it is a self-calibrated technique in terms of transmission; dividing a spectrum obtained during the occultation by a reference solar spectrum recorded outside the atmosphere removes the solar signature and leaves a transmittance containing only information about the composition of the Venus atmosphere. The reference spectrum is in fact defined by selecting spectra recorded between ~60 s and 90 s before the occultation effectively starts. However, to take the satellite drift into consideration, those spectra cannot be simply averaged. A linear regression on every pixel of the detector is performed so that the reference spectrum corresponding to an occultation spectrum taken at a given time includes the decrease (or increase) of solar intensity (see Fig. 13).

Figure 14 gives an example of the evolution of the spectra through one occultation (sunset 15 April 2007) in the orders 121, 149, 171, and 190 corresponding to the 2725–2750 cm<sup>-1</sup>, 3330–3357 cm<sup>-1</sup>, 3820–3855 cm<sup>-1</sup>, and 4245–4283 cm<sup>-1</sup> ranges, respectively. These transmittances show the characteristic behavior observed on all occultation series measured by SOIR. At the beginning of the series, the light path does not cross the atmosphere. No absorption signatures are present and transmittances are equal to unity. As the Sun sets, the light path goes deeper and deeper into the atmosphere, and two absorption processes take place; the overall signal decreases due to extinction by aerosols and absorption

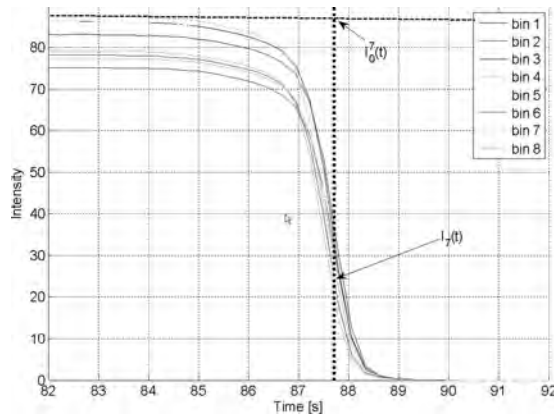


Fig. 13. Evolution in time of the signal intensity (sunset 3 September 2006). The plotted intensity is an average value over all 320 pixels (wavelengths) for each of the recorded orders. The eight curves correspond to the eight spectra recorded in 1 s (bin 1 and bin 2 part of the detector for each of the four selected orders). First direct solar radiation is measured when the light path does not cross the Venusian atmosphere. During the occultation, the observed signal decreases. Finally, the light path is intercepted by the cloud cover lying at 60–65 km and no light reaches the detector anymore. The dashed line shows the linear regression representing the solar reference spectrum. At time  $t$ , the observed signal is  $I(t)$  corresponding to an effective reference spectrum  $I_0(t)$ .

signatures appear. At the end of the observation, no light is captured anymore, as the Sun disappears behind the cloud deck or moves out of SOIR's field of view due to diffraction. The structures seen in the spectra of Fig. 14 are mainly attributed to HDO [Fig. 14(a)], CO<sub>2</sub> [Fig. 14(b)], H<sub>2</sub>O [Fig. 14(c)] and CO [Fig. 14(d)]. From this figure, it can also be seen that in general, the SOIR spectra contain information on the Venus atmosphere between 65 and 110 km for molecules such as HDO or HCl. For H<sub>2</sub>O and CO, signatures are still observable up to 130 km of altitude and CO<sub>2</sub> features are seen up to 125–130 km [11,12]!

The retrieval code allowing the determination of the vertical profiles of the different observed species is based on the onion-peeling method, starting the analysis of a series of spectra of an occultation with the spectrum corresponding to the highest altitude where a signature is visible, deriving the concentration in that most external layer and using this information for analyzing the next spectrum of the series. Progressively, the vertical profile is constructed from the most external layer down to an altitude of 65 km. The full description of this procedure will be presented in a forthcoming paper [13].

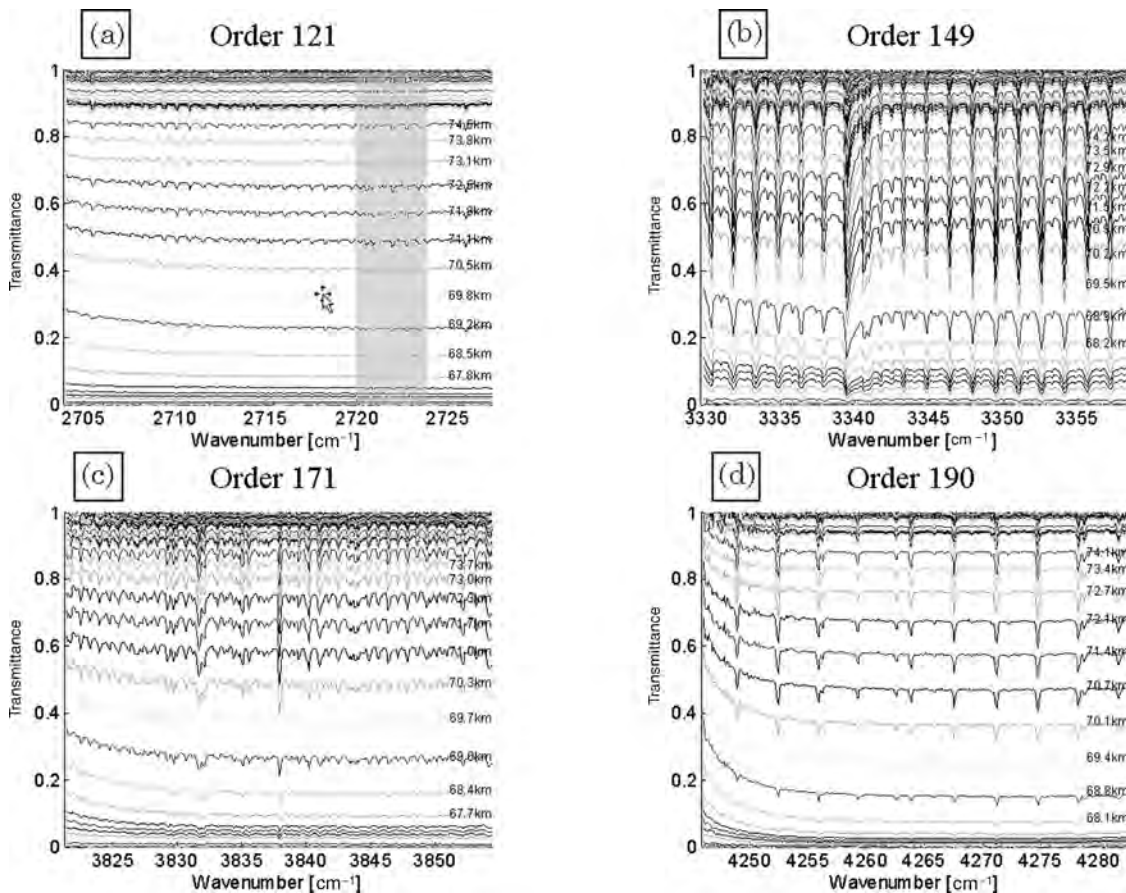


Fig. 14. Example of spectra obtained during one occultation (sunset 15 April 2007). Each transmittance is obtained by taking the ratio of the solar spectrum seen through the Venus atmosphere to the nonattenuated solar spectrum measured above the atmosphere. The selection of a spectral interval is achieved through the AOTF, tuned in this case to (a) 15 809 kHz for diffraction order 121, (b) 19 869 kHz for diffraction order 149, (c) 23 031 kHz for diffraction order 171, (d) 25 742 kHz for diffraction order 121. In these particular ranges of wavenumber, the main absorption lines are from (a) HDO, (b) CO<sub>2</sub>, (c) H<sub>2</sub>O, (d) CO.

## 7. Conclusions

SOIR is a sensitive instrument placed onboard Venus Express (ESA). It combines an echelle grating spectrometer and an AOTF, the latter being used for the selection of the appropriate grating orders. SOIR performs solar occultation measurements in the IR region (2.2–4.3  $\mu\text{m}$ ) and is, therefore, sensitive to the absorption of some key gases for the chemistry of the atmosphere of Venus, such as  $\text{H}_2\text{O}$ , CO and  $\text{CO}_2$ , and HDO, HCl, and HF, for which concentration vertical profiles were obtained for the first time [14].

The in-flight performance of the instrument has been examined in detail. In particular the corrections for the thermal and dark currents and for the non-linearity of the detector are taken into account. In-flight measurements have allowed the determination of the pixel-to-pixel variability of the detector, describing the slight difference of the physical properties of each pixel of the detector. The overall spectral sensitivity of the instrument has also been investigated. From dedicated measurements of well-defined and isolated solar lines, the characteristics of the AOTF could be inferred. In particular, the wavenumber versus AOTF frequency relation has been obtained for the different configurations of the instrument. The AOTF bandpass functions have been obtained from several solar lines, allowing for determination of this function over the entire spectral domain.

Finally, the precise analysis of some well-chosen solar lines led to a better definition of the instrumental resolution and its evolution over the spectral domain investigated by the instrument. Solar occultation measurement is a self-calibrated technique in terms of transmission, as it corresponds to the division of two spectra, one obtained while looking at the Sun through the atmosphere and one recorded outside the atmosphere. Preliminary analysis has shown the possibility to retrieve vertical profiles between 65 and 120 km for most of the observed species.

The research program was supported by the Belgian Federal Science Policy Office and the European Space Agency (ESA Programme for the Development of Scientific Experiments, contracts C 90 268, 90 113, and 17 645). Procurement of the AOTF was funded by Centre National d'Etudes Spatiales. We thank Jacques Sauval of the Royal Observatory, Brussels, Belgium, who provided us with a catalog of the solar absorption lines for the wavenumber range of interest. The Russian team also acknowledges Russian Foundation for Basic Research grant 06-02-72563.

## References

1. J. L. Bertaux, D. Fonteyn, O. Korablev, E. Chassefière, E. Dimarellis, J. P. Dubois, A. Hauchecorne, M. Cabane, P. Rannou, A. C. Lévassieur-Regourd, G. Cernogora, E. Quémerais, C. Hermans, G. Kockarts, C. Lippens, M. De Mazière, D. Moreau, C. Muller, B. Neefs, P. C. Simon, F. Forget, F. Hourdin, O. Talagrand, V. I. Moroz, A. V. Rodin,

- B. Sandel, and A. Stern, "The study of the Martian atmosphere from top to bottom with SPICAM light on Mars Express," *Planet. Space Sci.* **48**, 1303–1320 (2000).
2. J. L. Bertaux, D. Nevejans, O. Korablev, E. Villard, E. Quémerais, E. Neefs, F. Montmessin, F. Leblanc, J. P. Dubois, and E. Dimarellis, "SPICAV on Venus Express: three spectrometers to study the global structure and composition of the Venus atmosphere," *Planet. Space Sci.* **55**, 1673–1700 (2007).
3. D. V. Titov, H. Svedhem, D. Koschny, R. Hoofs, S. Barabash, J.-L. Bertaux, P. Drossart, V. Formisano, B. Häusler, O. Korablev, W. J. Markiewicz, D. Nevejans, M. Pätzold, G. Piccioni, T. L. Zhang, D. Merritt, O. Witasse, J. Zender, A. Accomazzo, and M. Sweeney *et al.*, "Venus Express science planning," *Planet. Space Sci.* **54**, 1279–1297 (2006).
4. D. Nevejans, E. Neefs, E. Van Ransbeeck, S. Berkenbosch, R. Clairquin, L. De Vos, W. Moelans, S. Glorieux, A. Baeke, O. Korablev, I. Vinogradov, Y. Kalinnikov, B. Bach, J.-P. Dubois, and E. Villard, "Compact high-resolution space-borne echelle grating spectrometer with AOTF based on order sorting for the infrared domain from 2.2 to 4.3 micrometer," *Appl. Opt.* **45**, 5191–5206 (2006).
5. A. C. Vandaele, M. De Mazière, R. Drummond, A. Mahieux, E. Neefs, V. Wilquet, D. Belayev, A. Fedorova, O. Korablev, F. Montmessin, and J.-L. Bertaux are preparing a manuscript to be called "Composition of the Venus mesosphere measured by SOIR onboard Venus Express."
6. C.-C. Hsieh, C.-Y. Wu, F.-W. Jih, and T.-P. Sun, "Focal-plane-arrays and CMOS readout techniques of infrared imaging systems," *IEEE Trans. Circuits Syst. Video Technol.* **7**, 594–605 (1997).
7. I. C. Chang, "Acousto-optic tunable filters," in *Acousto-Optic Signal Processing: Theory and Implementation*, N. Berg and J. Pellegrino, eds. (Marcel Dekker, 1996).
8. N. Uchida, "Optical properties of single-crystal paratellurite ( $\text{TeO}_2$ )," *Phys. Rev. B* **4**, 3736–3745 (1971).
9. T. Yano and A. Watanabe, "Acoustooptic  $\text{TeO}_2$  tunable filter using far-off-axis anisotropic Bragg diffraction," *Appl. Opt.* **15**, 2250–2258 (1976).
10. F. Hase, P. Demoulin, A. J. Sauval, G. C. Toon, P. F. Bernath, A. Goldman, J. W. Hannigan, and C. P. Rinsland, "An empirical line-by-line model for the infrared solar transmittance spectrum from 700 to 5000  $\text{cm}^{-1}$ ," *J. Quant. Spectrosc. Radiat. Transfer* **102**, 450–463 (2006).
11. J.-L. Bertaux, A. C. Vandaele, V. Wilquet, F. Montmessin, R. Dahoo, E. Villard, O. Korablev, and A. Fedorova, "First observation of 628  $\text{CO}_2$  isotopologue band at 3.3  $\mu\text{m}$  in the atmosphere of Venus by solar occultation from Venus Express," *Icarus* (2007), doi:10.1016/j.icarus.2008.01.001.
12. V. Wilquet, A. Mahieux, A. C. Vandaele, V. I. Perevalov, S. A. Tashkun, A. Fedorova, O. Korablev, F. Montmessin, R. Dahoo, and J.-L. Bertaux, "Line parameters for the 01111–00001 band of  $^{12}\text{C}^{16}\text{O}^{18}\text{O}$  from SOIR measurements of the Venus atmosphere," *J. Quant. Spectrosc. Radiat. Transfer* **109**, 895–905 (2008).
13. V. Wilquet, A. Mahieux, A. C. Vandaele, F. Montmessin, O. Korablev, A. Fedorova, and J.-L. Bertaux, "Characterization of the upper Venusian haze from UV to mid-IR by SPICAV/SOIR on Venus Express," *J. Geophys. Res.* (2008).
14. J.-L. Bertaux, A. C. Vandaele, O. Korablev, E. Villard, A. Fedorova, D. Fussen, E. Quémerais, D. Beliaev, A. Mahieux, F. Montmessin, C. Müller, E. Neefs, D. Nevejans, V. Wilquet, J. P. Dubois, A. Hauchecorne, A. Stepanov, I. Vinogradov, R. A., and a. t. S. team, "A warm layer in Venus' cryosphere and high altitude measurements of HF, HCl,  $\text{H}_2\text{O}$  and HDO," *Nature* **450**, 646–649, doi:10.1038/nature05974 (2007).